# Phase-Sensitive Open-Path Dual-Comb Spectroscopy with Free-Running Combs

Xinyi Chen,[1,2] Chao Huang,[1] Jiarui Li,[1] Minjian Lu,[1] Yan Li,[1] and Haoyun Wei[1,*]

[1] *State Key Laboratory of Precision Measurement Technology & Instruments, Department of Precision Instrument, Tsinghua University, Beijing 100084, China*

[2] *Science and Technology on Metrology and Calibration Laboratory, Beijing Institute of Radio Metrology and Measurement, Beijing 100854, China*

(Received 12 November 2022; revised 28 February 2023; accepted 13 March 2023; published 6 April 2023)

Open-path dual-comb spectroscopy has emerged as a promising technique for regional multigas monitoring with its conspicuous advantages of broadband spectral coverage, high spectral resolution, and rapid update rate. However, it is challenging to realize its full potential due to the undesirable mutual coherence of the dual-comb source and turbulence in the air path, which hinder it from field-deployed open-path applications. Here, phase-sensitive open-path dual-comb spectroscopy based on free-running combs is reported, in which dual-purpose compensation is proposed to provide immunity against both the time jitter of comb sources and turbulent noise. Broadband and high-fidelity atmospheric amplitude and phase spectra containing gas absorption and dispersion information over a 900-m turbulent air path are acquired. For the rovibrational resonances of $CO_2$ and $H_2O$ in 6250–6660 $cm^{-1}$, the achieved residual of the amplitude spectrum is no more than 0.01, and the average residual of the phase spectrum is 0.2 mrad, corresponding to about 0.2 as of relative timing noise or a refraction-index change of about $6 \times 10^{-14}$ over the target path. The precision of concentration retrieval is about 3 ppm for $CO_2$ in 30 s. A simulated gas-leakage measurement validates the dynamic monitoring capability of this system. This highly effective noise-compensation method provides the possibility of deploying the portable configuration and holds the potential to propel environmental protection and atmospheric science.

DOI: 10.1103/PhysRevApplied.19.044016

## I. INTRODUCTION

Open-path measurements of atmospheric trace gases are essential for quantifying greenhouse gases, hazardous gases, and pollutants resulting from urban emissions [1], oil and gas production [2], and industrial operations [3]. The intrinsic advantages of dual-comb spectroscopy (DCS) [4–13]—broad spectral coverage, rapid update rate, and comb-tooth resolution—make it well suited to obtain an atmospheric spectrum of multiple gas species with high precision. Currently, DCS implemented on a mutually coherent phase-locked scheme provides a bright prospect for open-path spectrum measurements across kilometer-scale paths [14–17], and when combined with an airborne retroreflector or multiple paths, this technique has recently been demonstrated to enable spatial mapping [18] and regional emission attribution [19].

However, in open-path dual-comb measurements, for one thing, the time jitter of the light sources weakens the mutual coherence between the two free-running combs. The reported research all uses a mutually coherent phase-locked scheme [20,21], which leads to high-frequency stability of the sources with a stable optical reference, but the rigorous locking equipment greatly increases the complexity of the system. Atmospheric turbulence can easily lead to severe decoherence in interferometry, especially for demanding phase measurements, posing a distinct challenge in open-path spectroscopy [22–25]. To avoid this problem, non-phase-sensitive configurations are commonly employed in open-path DCS for common-mode noise suppression, in which the phase features providing molecular dispersive information are unavailable. A broadband atmospheric phase spectrum has only been acquired to date with a phase-compensation method [15] under the Taylor frozen-turbulence hypothesis [26]. It considers that DCS has the ability to achieve turbulence immunity on the timescale of a single interferogram, and thus, only interinterferogram phase alignment relative to a reference is performed. The intrainterferogram high-frequency noise introduced by turbulence has never been effectively compensated for.

Here, we propose a dual-purpose compensation method for phase-sensitive dual-comb spectroscopy over the open path, which is capable of simultaneously compensating for the time jitter of the comb sources and the turbulent disturbance within each interferogram. Based

*luckiwei@mail.tsinghua.edu.cn

 

on this dual-purpose compensation, high-fidelity intensity and phase features of atmospheric absorption are acquired using a free-running dual-comb spectrometer. Atmospheric spectra spanning from 6250 to 6660 $cm^{-1}$ are extracted over a turbulent air path of about 900 m. The residual of the amplitude spectrum is no more than 0.01 for the strong overlapping features of $CO_2$ and $H_2O$. Meanwhile, the average residual of the phase spectrum is 0.2 mrad, corresponding to about 0.2 as of relative timing noise or a refraction-index change of about $6 \times 10^{-14}$ over the target path. The achieved measurement precision (estimated as the Allan deviation) is about 3 parts per million (ppm) for $CO_2$ in 30 s. Furthermore, one field-test scenario simulating pipeline leakage is presented to demonstrate the capability of dynamic emission monitoring. The concentrations retrieved from the amplitude and phase spectra are in good agreement to 0.82 ppm.

## II. METHOD

In open-path measurements, turbulence is a significant challenge that induces intensity and phase noise in the propagation of the laser [22–24], severely degrading spectral quality. The intensity noise that directly results in the evident intermittent signal scintillation has attracted some attention [14,27]. In a single sampling period, it does not distort the spectrum and can allow for coherent averaging. During continuous sampling, it leads to drift of the beam position, causing fluctuations in the power of received light, as shown in Fig. 1(a). If there is notable attenuation, the interference signal with a too-low signal-to-noise ratio (SNR) needs to be discarded, as in Ref. [14]. More importantly, turbulent phase noise leads to a significant pulse wander for the signal comb in the phase-sensitive DCS configuration. Under this circumstance, atmospheric turbulence will drive severe decoherence between the signal comb and the local oscillator (LO) comb, which can directly distort the interferometry measurements.

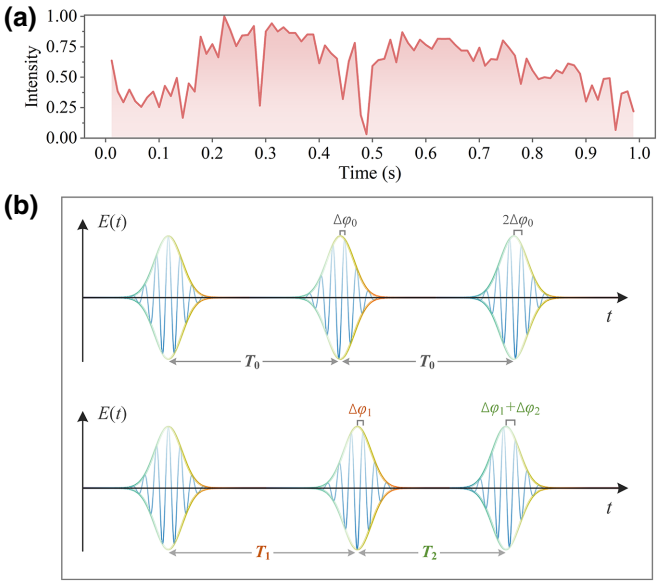


FIG. 1. Schematic of turbulent noise. (a) Turbulence-intensity noise; (b) turbulence phase noise. Top, ideal pulse train; bottom, pulse train affected by turbulence.

The turbulent phase noise can be expressed as $\delta\phi(t) = 2\pi\lambda_0{}^{-1}\delta x(t)$. $\lambda_0$ is the optical carrier wavelength. $\delta x(t)$ is the variation in the optical path length, as $\delta x(t) = \int_0^L \delta n(z, t)dz$, where $L$ is the total path length and $z$ is the beam-propagation direction. For an optical carrier, $\delta n(z, t)$ is the variation in the phase refraction index. Turbulent phase noise essentially arises from the time-dependent fluctuations of the atmospheric refraction index. Therefore, it is reasonable to restrain atmospheric decoherence by quantified compensation for the turbulence-induced refraction-index variations to realize high-quality spectra. The effects of refraction-index variations can be divided into variations in zero-order, first-order, and higher-order terms of its derivative with respect to frequency. For the variation in the zero-order term, it leads to a gradually changing carrier phase relative to the pulse envelope, $\Delta\varphi_0$. For the variation in the first-order term, it leads to fluctuations in the group refraction index that dominates the pulse-to-pulse arrival time, $T_0$. The effects of the zero-order and first-order terms are visually expressed in Fig. 1(b). For the variation in the higher-order term, it leads to intrapulse temporal broadening. Referring to research on turbulence [23–25], the time jitter caused by the dispersion in the case of the picosecond-level pulse width and kilometer-level path length is negligible.

To verify the above theoretical analysis, the relative linewidth between the dual-comb source and the phase of the dual-comb interference signal before and after passing through the atmosphere are compared. The radio-frequency spectra of one pair of comb teeth are shown in Fig. 2(a). After the transmission, the relative linewidth between the two free-running combs is further broadened due to the time jitter caused by the turbulent phase noise, which induces lower resolution. Additionally, in an ideal situation, the phase of the dual-comb interference signal should maintain a linear increase over time. The deviation between the actual phase and the theoretical linear value is shown in Fig. 2(b). The phase of the interference signal between the two free-running combs fluctuates randomly due to the source-induced time jitter, and turbulence further aggravates this phase fluctuation, which results in more serious distortion of the interference signals.

According to the above analysis and verification, variations in the carrier phase and the pulse time of flight caused by the turbulent phase noise can be equivalent to the influence of the jitter in the carrier-envelope offset and repetition frequency of the combs. In the DCS, two diode lasers are used wisely as intermediates for coherence-information extraction of the comb sources [28]. The jitter of the

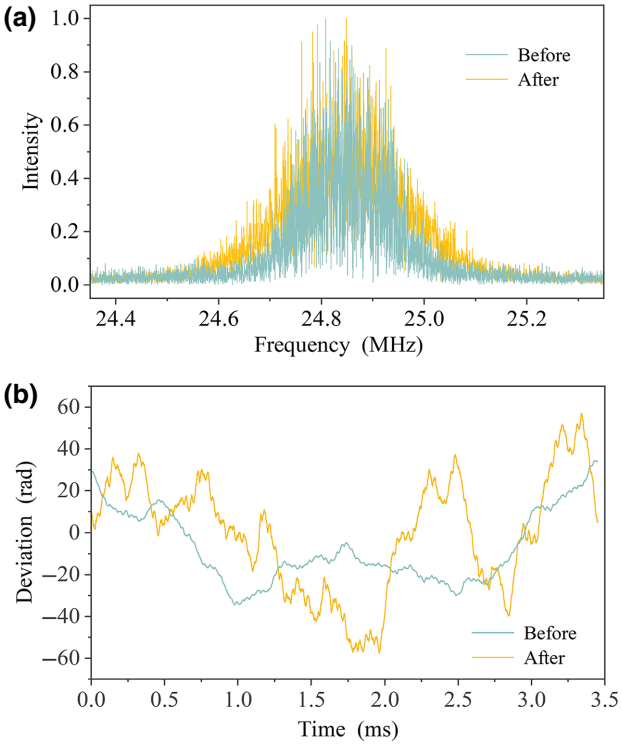


FIG. 2. Verification of the turbulence-induced influence on the dual-comb interference. Comparison of the results before (green) and after (yellow) passing through the atmosphere (well-mixed conditions, wind speeds of ∼1–3 m/s, path length of ∼900 m). (a) Relative linewidth of the dual-comb source; (b) deviation between the phase of the dual-comb interference signal and theoretical linear values.

two frequency parameters of the comb can be compensated for using the interference signals between the diode lasers and the combs [29,30]. In the phase-sensitive open-path DCS configuration, the frequency stability of the dual-comb source can be indirectly improved by digital compensation with two diode lasers. Simultaneously, without additional data, the impact of the turbulent phase noise can also be suppressed by following a similar digital approach. Specifically, the signal comb returning from the air path is used to interfere with the diode lasers. The interference signals containing both turbulence-induced and source-induced jitter information are utilized to realize dual-purpose compensation through a digital algorithm during data postprocessing. The interference between a comb and a diode laser produces two sets of beat notes ($nf_r \pm f_{\text{beat}}$, $nf_r - f_{\text{beat}}$), and only the beat note at the lowest frequency ($f_{\text{beat}}$) is selected by a low-pass filter. Four filtered beat notes between the two combs and the diode lasers constitute the compensation signal, which can be employed to extract coherence information of the signal and LO combs, and then the information can be used to perform phase correction and linear-sampling reconstruction for dual-comb interferograms. As a result, the influence of turbulence-induced and source-induced jitter is compensated for and the distortions of the interferograms are recovered. In addition, each individual sample in the interferogram is compensated for by the corresponding compensation signal. Therefore, intrainterferogram high-frequency turbulent phase noise can also be suppressed. In general, dual-purpose compensation for intrainterferogram turbulence-induced and source-induced jitter can be achieved simultaneously, enabling open-path atmospheric-absorption-spectrum detection using free-running combs.

## III. SETUP

The setup for the phase-sensitive open-path DCS with free-running combs is illustrated in Fig. 3. The system consists of two free-running erbium-doped-fiber frequency combs, with a repetition frequency, $f_r$, of about 250 MHz that differ by $\Delta f_r$ (difference in comb repetition frequency, 290 Hz). The signal and LO combs cover 6250–6660 $\text{cm}^{-1}$ (1.5–1.6 μm), overlapping with $CO_2$ and $H_2O$ bands. No feedback signal is input into either the signal or LO comb for phase-locked control. The signal comb is transmitted by a single-mode fiber to the transceiver unit located in an outdoor cabinet with fixable casters. At the transceiver unit, the signal comb is collimated by a reflective collimator (diameter, 8 mm) after passing through a fiber circulator. The beam is then expanded by a pair of off-axis parabolic mirrors (OPMs; diameter, 1″, 4″; focal length, 1″, 4″). The signal comb is launched as a Gaussian beam with a diameter of 32 mm and about 5-mW power. The unit is an all-reflective design to allow broadband measurements. A 900-m roundtrip open path on the campus is extended between this unit and a 2″-diameter hollow retroreflector at the far end. The current path length is limited by the road conditions, while the efficiency of the transceiver holds the potential for longer-distance detection. In the phase-sensitive DCS configuration, only the signal comb is transmitted over the turbulent air path. The retroreflected light is received by the same unit and finally collected into a single-mode fiber.

The return-signal comb is split into two parts, of which one is used for dual-purpose compensation and the other is used for interfering with the LO comb. Since we finely align the main adjustable optics (the two OPMs and the retroreflector), the received optical power has a typical level of about 0.2–0.9 mW (at wind speeds of ∼1–3 m/s) and can support the needs of the above two parts. For the compensation part, the basic unit is a portable module composed of all-fiber components. As discussed in Sec. II, two narrow-linewidth diode lasers (1534.223 and 1564.701 nm) are used for compensation-signal extraction. For the interference part, the two combs are combined by a 95:5 fiber combiner, and then the interference signal is recorded by a detector [(In, Ga)As, 150 MHz]. One fiber polarization controller is used to control the polarization

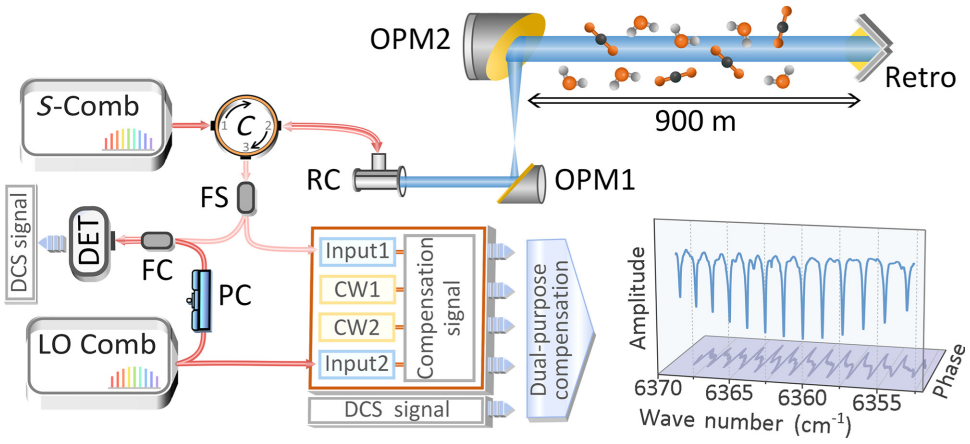


FIG. 3. Experimental setup for phase-sensitive open-path DCS with free-running combs. Signal comb (*S*-comb) is launched and collected by a transceiver unit (*C*, fiber circulator; RC, reflective collimator; OPM, off-axis parabolic mirror). Retro, corner-cube retroreflector; FS, fiber splitter; PC, polarization controller; FC, fiber combiner; DET, detector; CW, continuous-wave diode laser; Red, fiber; Light red, fiber that transmits the return light; Blue, air path.

of the LO comb to enhance the SNR of the interference signal. Finally, the compensation signal and interference signal are digitized by analog-to-digital converters (14 bits, 250 Msps) and then processed in a field-programmable gate array. The DCS signal is a series of interferograms that repeat every 3.4 ms (given by $1/\Delta f_r$). After dual-purpose compensation, the interferogram is then Fourier transformed to obtain a complex radio-frequency spectrum. The amplitude and phase spectrum of the atmosphere can be reproduced by frequency mapping of the radio-frequency spectrum.

## IV. RESULTS

### A. Comparison of dual-purpose and source-only compensation

For dual-comb measurements based on free-running sources, compensation for turbulent noise as well as comb-source jitter is crucial. The spectral measurement results of the dual-purpose compensation method for the phase-sensitive DCS (DP DCS), the source-only compensation method for phase-sensitive DCS (SP DCS), and the source-only compensation method for non-phase-sensitive DCS (SNP DCS) are compared here to illustrate the necessity of turbulent-noise compensation and the enhanced performance of the DP DCS method for open-path measurements. Since the SNP DCS method is incapable of phase-spectrum measurements, the transmission spectra measured by the three methods are compared in Fig. 4(a). The atmospheric transmission spectra are obtained by removing the spectral baseline structure from the amplitude spectra. In Fig. 4(a), the light-blue spectrum is the result of 1 s, and the red one is the result of 10-s average. The gray area corresponds to the theoretical spectral line position and full width at half maximum (FWHM) range. The power of the launched beam and the optics used in these three methods are almost the same.

The results of the SP DCS and DP DCS methods are compared in the top and bottom graphs in Fig. 4(a). For the SP DCS method, since the turbulence-induced noise for the signal comb still exists, it is almost impossible to distinguish the absorption lines, even for the 10-s-averaged result. In sharp contrast, for the DP DCS method, benefitting from effectively reconstructed interference signals, clear and complete absorption lines can be found in both single and averaged measurements. A more visual comparison of the amplitude spectra measured by these two methods is shown in Fig. 4(b). The poor performance of SP DCS makes the baseline rough and bumpy, as illustrated in the expanded view, which is the reason for no obvious signal. In fact, the baseline should be flat and smooth, which is determined by the characteristic of the light source, as manifested in the DP DCS. The high-SNR measurements of DP DCS well reproduce the baseline structure and fine absorption lines of $CO_2$ and $H_2O$ in this band, as shown in the inset.

The middle and bottom graphs in Fig. 4(a) compare the performance of the SNP DCS and DP DCS methods. For the SNP DCS method, the real-time variation of the optical path length introduced by turbulence leads to the unequal sampling of the interferogram on the detector, which significantly broadens the spectral lines and obviously shifts the line positions. Instead, for the DP DCS method, absorption lines with stable positions and FWHMs that match theoretical calculation are obtained in both single and averaged measurements. A quantitative comparison of the deviations of the spectral line positions of these two methods is shown in Fig. 4(c). The average position deviation of SNP DCS is almost 2 orders of magnitude larger than that of DP DCS, which is far behind the expected accuracy

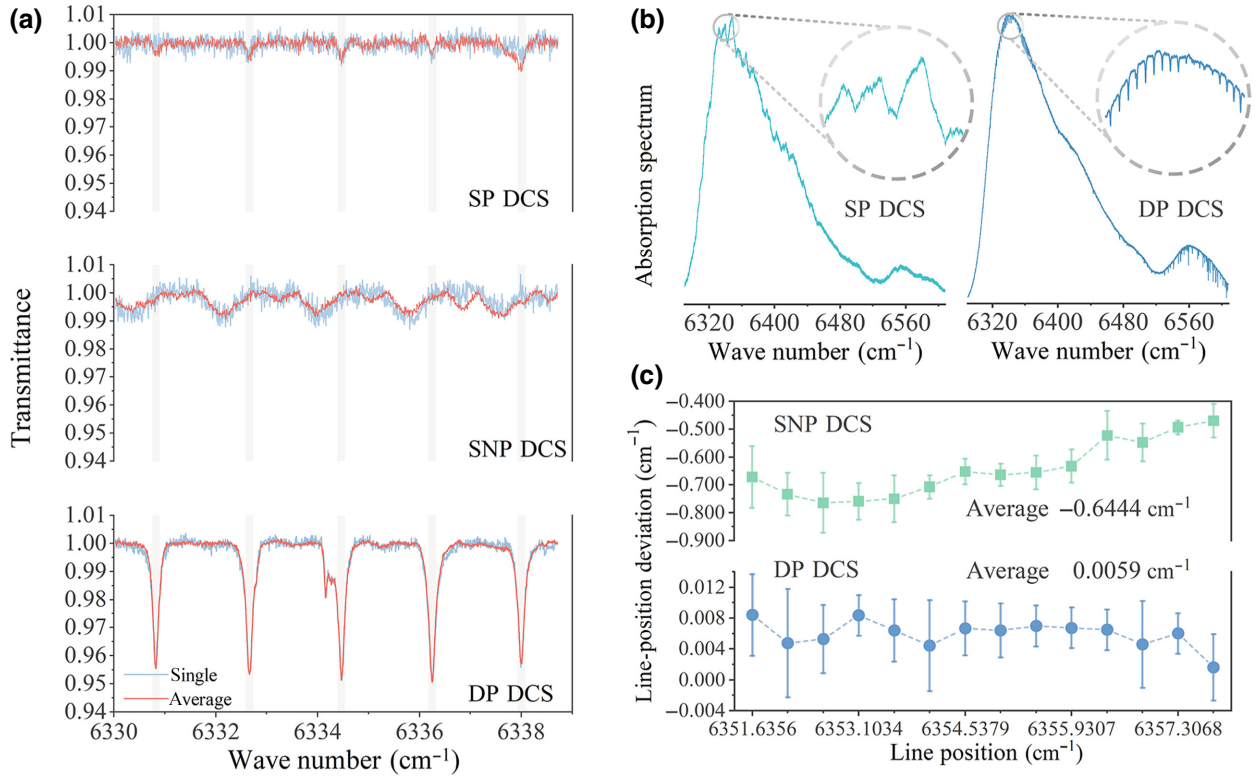


FIG. 4. Comparison of atmospheric spectra obtained by the SP DCS, SNP DCS, and DP DCS methods. (a) Transmission spectra measured by the three methods. (b) Amplitude spectra measured by the SP DCS and DP DCS methods. (c) Deviations of the spectral line positions of the SNP DCS and DP DCS methods.

of DCS. Therefore, SNP DCS is incapable of gas identification, let alone emission quantification. In a word, for the free-running dual-comb spectrometer, the source-only compensation method is unable to support open-path measurements, and the dual-purpose compensation method is a valid technique for turbulent-noise suppression.

### B. Results of atmospheric-absorption-amplitude and phase spectra

Spectral detection of atmospheric mixtures is performed across a window of about 400 cm$^{-1}$ in the range of near-infrared. Measured spectra span about 50 000 comb teeth and data are acquired at a comb-tooth separation of about 0.0083 cm$^{-1}$ (250 MHz) with negligible instrument line shape. Figure 5(a) shows the acquired broadband amplitude spectrum. The SNR in the spectral domain is about 4000 for 1-min coherent averaged data. Magnifying the spectrum, fine absorption lines can be found in the expanded layouts.

Furthermore, the transmission and phase spectra over a spectral window of about a 45 m$^{-1}$, containing the 30 012 ← 00 001 combination band of $CO_2$, are shown in Figs. 5(b) and 5(c). It should be noted that the transmission spectrum is obtained via a critical piecewise baseline fitting, while the phase spectrum is baseline free. The inherent advantage of the phase spectrum provides it with the potentiality to quantify molecular absorption more flexibly without additional baseline correction.

To quantitatively characterize the measurement performance, Figs. 5(d) and 5(e) show the experimental and theoretical calculation results within a narrow spectral window that includes obvious resonances of $CO_2$ and $H_2O$. The typical trace gas-absorption lines of about 0.15 cm$^{-1}$ are well demonstrated with about 16 teeth apiece, indicating that both the amplitude and phase spectra are in good agreement with theoretical calculations. For the strong overlapping absorption features, the residual of transmittance is no more than 0.01, which benefits from aggressive baseline fitting. In the range of Fig. 5(e), the maximum residual of the phase spectrum is 1.8 mrad. The average residual is 0.2 mrad, corresponding to about 0.2 as of relative timing noise or a refraction-index change of about $6 \times 10^{-14}$ over the target path; these values are comparable with a report on open-path phase-spectrum measurements based on a mutually coherent phase-locked scheme [15]. The residuals (especially for transmittance) exhibit fluctuations near the center of the spectral line, which can be attributed to optimizable line parameters, line-shape models, and line-mixing effects [14,17,31].

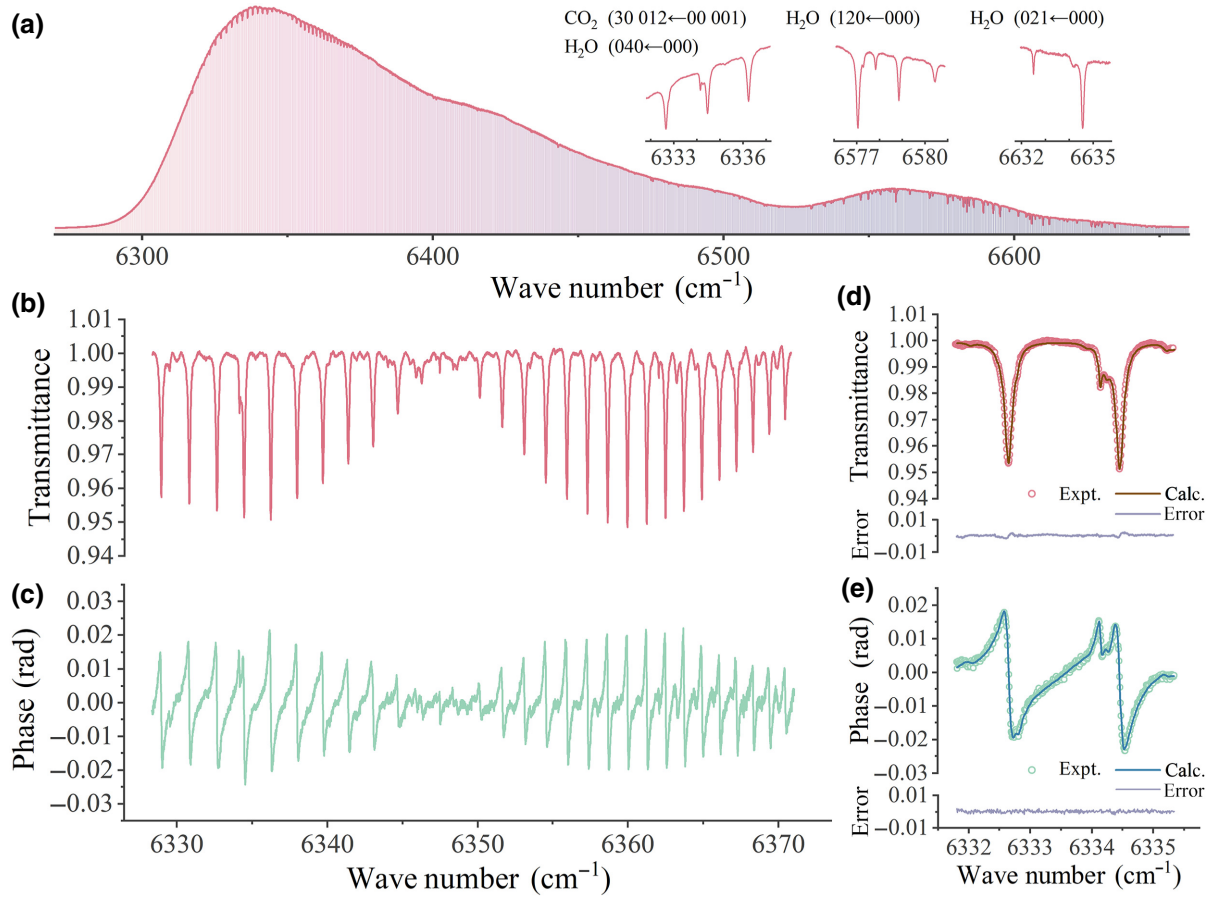


FIG. 5. Broadband atmospheric amplitude and phase-spectra measurements. (a) Amplitude spectrum with expanded layouts for fine absorption lines of different rovibrational levels. (b),(c) Transmission and phase spectra of the 30 012 ← 00 001 combination band of $CO_2$. (d),(e) Expanded windows of (b),(c) that include obvious feature overlap with $H_2O$.

The precision of this system for the relatively stable path-averaged concentration is estimated using the Allan deviation of the retrieved results from the amplitude and phase spectra. The precision is about 3 ppm for $CO_2$ in 30 s with the phase-spectrum measurement, which is on an equivalent level to the amplitude spectrum. A longer averaging time may result in higher precision, and the optimal averaging period depends on the atmospheric conditions [19]. In addition to the averaging time, the precision relates to gas-absorption intensity and inversion accuracy. For a stronger absorption intensity, one expects a longer operation distance and a longer wavelength in the mid-infrared region. For a higher concentration accuracy, several advances can support more reliable spectral inversion, such as more-efficient baseline extraction and etalon-suppression approaches [14,18]. To demonstrate the dynamic monitoring capability of this system, which can be used for leakage detection, we set a simulated field scenario by artificially placing a controlled $CO_2$-release source in the middle of the test path. This system is used to monitor the escape process of the leaking gas. Escape is controlled with the help of a plastic pipe and other slow-release measures, so that the entire escape process is on the order of 100 s. Finally, the dynamic quantitative emission monitoring of the release source is realized by detecting the change of the path-averaged concentration.

The path-averaged $CO_2$ concentrations versus time, which are retrieved by fitting the transmission and phase spectra to the complex gas-absorption model, are shown in Fig. 6(a). Each point in the curve is extracted from 1-s-averaged data. Since the gas concentration changes rapidly at the beginning, the selected measurement time interval is about 10 s, and the interval increases as the concentration change slows down. For this system, the gas-escape rate barely affects the spectral measurement reliability, and the spectral domain SNR of the 1-s data is maintained at about 550 throughout the monitoring process. The average deviation between the result extracted from the amplitude spectrum and that from the phase spectrum is 0.82 ppm. The good agreement in $CO_2$ concentration demonstrates that the atmospheric phase spectrum qualifies for use in the quantitative monitoring of trace gases.

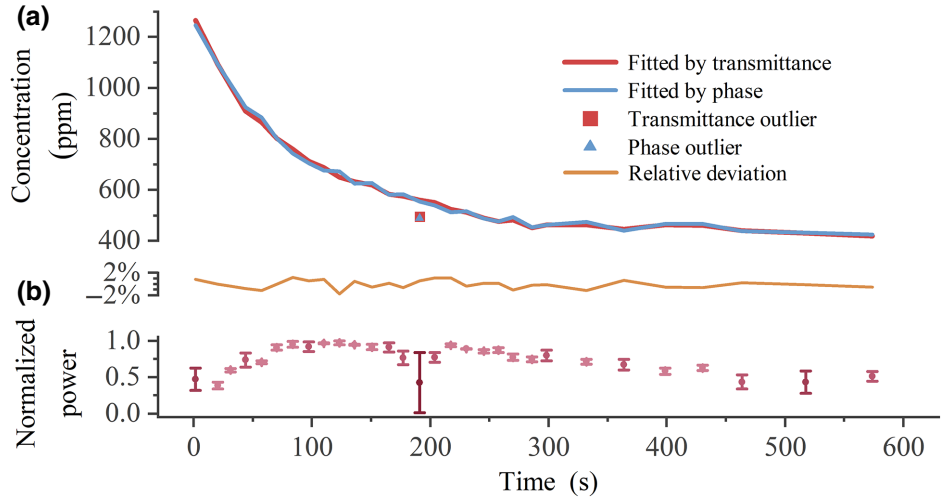


FIG. 6. Dynamic monitoring of $CO_2$ leakage. (a) Path-averaged $CO_2$ concentrations extracted from amplitude and phase spectra and relative deviation between the two results. (b) Normalized average power and standard deviation of the corresponding 1-s interference signals in (a).

Figure 6(b) shows the normalized average power and standard deviation of the interference signals within 1 s, corresponding to each point in Fig. 6(a). At about 190 s, the severe power fluctuation is due to vehicle obscuration. The corresponding point in the concentration-change curve is extracted after discarding the interferograms that are incomplete or drop too low. Outliers extracted without being discarded are shown as squares and triangles below the curves. During the test period, turbulence does induce power scintillation (such as 1 s, ∼520 s). Fortunately, this system can maintain a relatively reliable quantification ability, even in the case of undesirable received power. It can be seen that the dual-purpose compensation method can sufficiently suppress both the turbulence-induced and source-induced noise, supporting effective concentration inversion with accurate atmospheric amplitude and a phase spectrum containing comprehensive molecular absorption information.

## V. CONCLUSION

We demonstrate that the high-fidelity intensity and phase features of atmospheric absorption can be acquired using free-running combs with a dual-purpose compensation method. For future work, a reasonable evaluation of the accuracy of this system can be achieved with upgraded devices that are able to control the gas-emission rate and be calibrated with other reliable methods, such as tunable-diode-laser absorption spectroscopy, which our group is currently researching; meanwhile, a higher output power can support spatial multiplexing of the sources for field-deployed regional sensing [19,32,33]. For the mid-infrared DCS [34–36], a processing algorithm requiring no additional reference light source is proposed and attempts are used for open-path detection based on quantum cascade lasers [37]. However, this algorithm could be invalid for the higher-resolution fiber dual-comb system. Our dual-purpose compensation scheme is expected to contribute to digital compensation for a mid-infrared fiber dual-comb system based on difference-frequency generation [36]. With further improvement, it is expected that open-path DCS with dual-purpose compensation based on a compact and portable commercial dual-comb spectrometer, inheriting the intrinsic advantages of broad spectral coverage, rapid update rate, and high spectral resolution, can offer real-time and accurate gas-absorption information for environmental protection and atmospheric science.

## ACKNOWLEDGMENTS

This work is supported by the National Natural Science Foundation of China (Grant No. 62275138) and the National Natural Science Foundation of China (Grant No. 61775114).

## APPENDIX A

Starting from the phase disturbance introduced by atmospheric turbulence to the pulses of the comb in the time domain, the corresponding theoretical analysis is supplemented.

First, the pulse sequence of a comb in the time domain can be expressed as

$$e_{\text{in}}(t) = \sum_{n=1} A\left(t - \frac{n}{f_r}\right) \exp\left(i\omega_0 t + i2\pi n \frac{f_{\text{CEO}}}{f_r}\right), \quad \text{(A1)}$$

where $A$ is the electric field envelope of each pulse and is a function of time $t$, $f_r$ is the repetition frequency, $f_{\text{CEO}}$ is

the carrier-envelope offset, and $\omega_0$ is the central angular frequency of the comb. Based on this, the $n$th pulse in the time domain can be described as

$$e_{\mathrm{in},n}(t) = A\left(t - \frac{n}{f_r}\right)\exp\left(i\omega_0 t + i2\pi n\frac{f_{\mathrm{CEO}}}{f_r}\right). \quad \text{(A2)}$$

Let $E_{\mathrm{in},n}(\omega)$ denote the $n$th pulse in the frequency domain:

$$E_{\mathrm{in},\,n}(\omega) = \mathcal{F}\{e_{\mathrm{in},\,n}(t)\}, \quad \text{(A3)}$$

with $\mathscr{F}$ representing Fourier transform.

Since here the discussion is about the effect of phase disturbance introduced by atmospheric turbulence on the comb, the absorption of the transmitted open path is assumed to be zero for simplicity. The phase shift of the $n$th pulse after passing through the open path can be decomposed into the ideal phase shift, $\psi_{\mathrm{ideal}}$, and the turbulent phase shift, $\psi_{\mathrm{tur},n}$:

$$\psi_n(\omega) = \psi_{\mathrm{ideal}}(\omega) + \psi_{\mathrm{tur},\,n}(\omega). \quad \text{(A4)}$$

Note that the turbulent phase shift, $\psi_{\mathrm{tur},n}$, is different from pulse to pulse, as indicated by subscript $n$, while the ideal phase shift, $\psi_{\mathrm{ideal}}$, remains constant for each pulse. Equation (A4) can be rewritten according to the Taylor expansions:

$$\begin{aligned}\psi_n(\omega) \approx{}& \psi_{\mathrm{ideal}}(\omega_0) + \frac{\partial\psi_{\mathrm{ideal}}}{\partial\omega}(\omega-\omega_0) + \ldots \\ &\psi_{\mathrm{tur},\,n}(\omega_0) + \frac{\partial\psi_{\mathrm{tur},\,n}}{\partial\omega}(\omega-\omega_0),\end{aligned} \quad \text{(A5)}$$

with all derivatives evaluated at $\omega = \omega_0$. Here, the ideal phase shift does not introduce any dispersion, and the turbulence also has a negligible dispersive effect. Therefore, the above Taylor expansions of both the ideal and turbulent phase shifts retain only the first-two terms. Higher-order terms for dispersive effect are not considered.

Based on the above expressions of comb pulses and phase shift, the $n$th pulse after passing through an open path (represented by "out") in the time domain can be described as [38]

$$\begin{aligned}e_{\mathrm{out},\,n}(t) = \mathcal{F}^{-1}\{E_{\mathrm{in},\,n}(\omega)\exp[i\psi_n(\omega)]\},{}& = \mathcal{F}^{-1}\left\{E_{\mathrm{in},\,n}(\omega)\exp\left(i\begin{bmatrix}\psi_{\mathrm{ideal}}(\omega_0) + \frac{\partial\psi_{\mathrm{ideal}}}{\partial\omega}(\omega-\omega_0) + \cdots \\ \psi_{\mathrm{tur},\,n}(\omega_0) + \frac{\partial\psi_{\mathrm{tur},\,n}}{\partial\omega}(\omega-\omega_0)\end{bmatrix}\right)\right\}, \\ &= \exp\left\{i\left[\psi_{\mathrm{ideal}}(\omega_0) - \frac{\partial\psi_{\mathrm{ideal}}}{\partial\omega}\omega_0 + \psi_{\mathrm{tur},\,n}(\omega_0) - \frac{\partial\psi_{\mathrm{tur},\,n}}{\partial\omega}\omega_0\right]\right\} \\ &\times \mathcal{F}^{-1}\left\{E_{\mathrm{in},\,n}(\omega)\left[\exp\left(i\omega\left(\frac{\partial\psi_{\mathrm{ideal}}}{\partial\omega} + \frac{\partial\psi_{\mathrm{tur},\,n}}{\partial\omega}\right)\right)\right]\right\}.\end{aligned} \quad \text{(A6)}$$

By using the property of Fourier transform, we have

$$\begin{aligned}e_{\mathrm{out},\,n}(t) = \exp&\left\{i\begin{bmatrix}\psi_{\mathrm{ideal}}(\omega_0) - \frac{\partial\psi_{\mathrm{ideal}}}{\partial\omega}\omega_0 + \ldots \\ \psi_{\mathrm{tur},\,n}(\omega_0) - \frac{\partial\psi_{\mathrm{tur},\,n}}{\partial\omega}\omega_0\end{bmatrix}\right\} \\ &\times e_{\mathrm{in},\,n}\left(t + \frac{\partial\psi_{\mathrm{ideal}}}{\partial\omega} + \frac{\partial\psi_{\mathrm{tur},\,n}}{\partial\omega}\right),\end{aligned} \quad \text{(A7)}$$

By combining Eq. (A7) with Eq. (A2), we can finally obtain

$$\begin{aligned}e_{\mathrm{out},\,n}(t) = \exp&\left\{i\begin{bmatrix}\omega_0 t + 2\pi n\frac{f_{\mathrm{CEO}}}{f_r} + \ldots \\ \psi_{\mathrm{ideal}}(\omega_0) + \psi_{\mathrm{tur},\,n}(\omega_0)\end{bmatrix}\right\} \\ &\times A\left(t + \frac{\partial\psi_{\mathrm{ideal}}}{\partial\omega} + \frac{\partial\psi_{\mathrm{tur},\,n}}{\partial\omega} - \frac{n}{f_r}\right),\end{aligned} \quad \text{(A8)}$$

According to the output-electric-field expression, Eq. (A8), the ideal phase shift of the open path introduces to the $n$th pulse a phase shift, $\psi_{\mathrm{ideal}}(\omega_0)$, and a time shift, $-(\partial\psi_{\mathrm{ideal}}/\partial\omega)$, in the time domain, which is the effect of the passage of an ideal optical path. Similarly, the turbulent one introduces a phase shift, $\psi_{\mathrm{tur},n}(\omega_0)$, and a time shift, $-(\partial\psi_{\mathrm{tur},\,n}/\partial\omega)$. $\psi_{\mathrm{tur},n}(\omega_0)$ and $-(\partial\psi_{\mathrm{tur},\,n}/\partial\omega)$ of different pulses ($n = 1, 2, 3\ldots$) can be viewed as random variables. Therefore, it can be seen that the turbulent-phase noise leads to the jitter of the carrier phase and time of flight from pulse to pulse.

In fact, we can further define $\delta f_{r,n}$ such that

$$-\frac{n}{f_r + \delta f_{r,\,n}} = \frac{\partial\psi_{\mathrm{tur},\,n}}{\partial\omega} - \frac{n}{f_r}, \quad \text{(A9)}$$

which leads to

$$\delta f_{r,\,n} = \frac{n}{-(\partial\psi_{\mathrm{tur},\,n}/\partial\omega) + (n/f_r)} - f_r. \quad \text{(A10)}$$

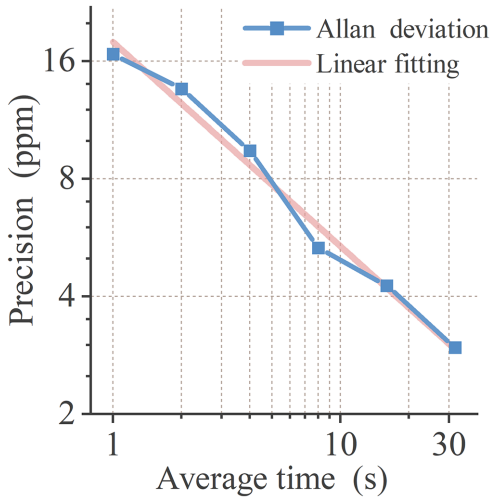


FIG. 7. Precision (Allan deviation) of the measurement for the relatively stable path-averaged $CO_2$ concentration without release.

Similarly, we define $\delta f_{\mathrm{CEO},n}$ such that

$$2\pi n\frac{f_{\mathrm{CEO}}+\delta f_{\mathrm{CEO},n}}{f_r+\delta f_{r,n}}=2\pi n\frac{f_{\mathrm{CEO}}}{f_r}+\psi_{\mathrm{tur},n}(\omega_0), \quad \text{(A11)}$$

which leads to

$$\delta f_{\mathrm{CEO},n}=(f_r+\delta f_{r,n})\frac{\psi_{\mathrm{tur},n}(\omega_0)}{2\pi n}+\delta f_{r,n}\frac{f_{\mathrm{CEO}}}{f_r}. \quad \text{(A12)}$$

Then, combining Eqs. (A8), (A9), and (A11), we can explicitly express the turbulent-phase shift in terms of the jitters of $f_r$ and $f_{\mathrm{CEO}}$ for each pulse:

$$e_{\mathrm{out},n}(t)=\exp\left\{i\left[\omega_0 t+2\pi n\frac{f_{\mathrm{CEO}}+\delta f_{\mathrm{CEO},n}}{f_r}+\ldots\right]\right\}\times A\left(t+\frac{\partial\psi_{\mathrm{ideal}}}{\partial\omega}-\frac{n}{f_r+\delta f_{\mathrm{r},n}}\right), \quad \text{(A13)}$$

with jitters $\delta f_{r,n}$ and $\delta f_{\mathrm{CEO},n}$ being related to $\psi_{\mathrm{tur},n}(\omega_0)$ and $\partial\psi_{\mathrm{tur},n}/\partial\omega$ by Eqs. (A10) and (A12).

## APPENDIX B

The Allan deviation of the obtained gas concentration versus the average time is shown to demonstrate the measurement precision of this free-running dual-comb system with the dual-purpose compensation method (Fig. 7).


[1] C. Le Quere, M. R. Raupach, J. G. Canadell, G. Marland, L. Bopp, P. Ciais, T. J. Conway, S. C. Doney, R. A. Feely, P. Foster, *et al.*, Trends in the sources and sinks of carbon dioxide, Nat. Geosci. **2**, 831 (2009).

[2] D. R. Caulton, P. B. Shepson, R. L. Santoro, J. P. Sparks, R. W. Howarth, A. R. Ingraffea, M. O. L. Cambaliza, C. Sweeney, A. Karion, K. J. Davis, *et al.*, Toward a better understanding and quantification of methane emissions from shale gas development, Proc. Natl. Acad. Sci. U. S. A. **111**, 6237 (2014).

[3] G. Petron, G. Frost, B. R. Miller, A. I. Hirsch, S. A. Montzka, A. Karion, M. Trainer, C. Sweeney, A. E. Andrews, L. Miller, *et al.*, Hydrocarbon emissions characterization in the Colorado Front Range: A pilot study, J. Geophys. Res.: Atmos. **117**, D04304 (2012).

[4] A. Schliesser, M. Brehm, F. Keilmann, and D. W. van der Weide, Frequency-comb infrared spectrometer for rapid, remote chemical sensing, Opt. Express **13**, 9029 (2005).

[5] I. Coddington, N. Newbury, and W. Swann, Dual-comb spectroscopy, Optica **3**, 414 (2016).

[6] B. Bernhardt, A. Ozawa, P. Jacquet, M. Jacquey, Y. Kobayashi, T. Udem, R. Holzwarth, G. Guelachvili, T. W. Hansch, and N. Picque, Cavity-enhanced dual-comb spectroscopy, Nat. Photonics **4**, 55 (2010).

[7] E. Baumann, F. R. Giorgetta, W. C. Swann, A. M. Zolot, I. Coddington, and N. R. Newbury, Spectroscopy of the methane $\upsilon_3$ band with an accurate midinfrared coherent dual-comb spectrometer, Phys. Rev. A **84**, 062513 (2011).

[8] T. Ideguchi, A. Poisson, G. Guelachvili, N. Picque, and T. W. Hansch, Adaptive real-time dual-comb spectroscopy, Nat. Commun. **5**, 3375 (2014).

[9] G. Villares, A. Hugi, S. Blaser, and J. Faist, Dual-comb spectroscopy based on quantum-cascade-laser frequency combs, Nat. Commun. **5**, 5192 (2014).

[10] Z. J. Chen, M. Yan, T. W. Hansch, and N. Picque, A phase-stable dual-comb interferometer, Nat. Commun. **9**, 3035 (2018).

[11] K. Xu, X. Zhao, Z. Wang, J. Chen, T. Li, Z. Zheng, and W. Ren, Multipass-assisted dual-comb gas sensor for multispecies detection using a free-running fiber laser, Appl. Phys. B: Lasers Opt. **126**, 1 (2020).

[12] A. Dutt, C. Joshi, X. C. Ji, J. Cardenas, Y. Okawachi, K. Luke, A. L. Gaeta, and M. Lipson, On-chip dual-comb source for spectroscopy, Sci. Adv. **4**, e1701858 (2018).

[13] M. G. Suh, Q. F. Yang, K. Y. Yang, X. Yi, and K. J. Vahala, Microresonator soliton dual-comb spectroscopy, Science **354**, 600 (2016).

[14] G. B. Rieker, F. R. Giorgetta, W. C. Swann, J. Kofler, A. M. Zolot, L. C. Sinclair, E. Baumann, C. Cromer, G. Petron, C. Sweeney, *et al.*, Frequency-comb-based remote sensing of greenhouse gases over kilometer air paths, Optica **1**, 290 (2014).

[15] F. R. Giorgetta, G. B. Rieker, E. Baumann, W. C. Swann, L. C. Sinclair, J. Kofler, I. Coddington, and N. R. Newbury, Broadband Phase Spectroscopy over Turbulent Air Paths, Phys. Rev. Lett. **115**, 103901 (2015).

[16] E. M. Waxman, K. C. Cossel, G. W. Truong, F. R. Giorgetta, W. C. Swann, S. Coburn, R. J. Wright, G. B. Rieker, I. Coddington, and N. R. Newbury, Intercomparison of open-path trace gas measurements with two dual-frequency-comb spectrometers, Atmos. Meas. Tech. **10**, 3295 (2017).

[17] G. Ycas, F. R. Giorgetta, K. C. Cossel, E. M. Waxman, E. Baumann, N. R. Newbury, and I. Coddington, Mid-infrared

dual-comb spectroscopy of volatile organic compounds across long open-air paths, Optica **6**, 165 (2019).

[18] K. C. Cossel, E. M. Waxman, F. R. Giorgetta, M. Cermak, I. R. Coddington, D. Hesselius, S. Ruben, W. C. Swann, G. W. Truong, G. B. Rieker, *et al.*, Open-path dual-comb spectroscopy to an airborne retroreflector, Optica **4**, 724 (2017).

[19] S. Coburn, C. B. Alden, R. Wright, K. Cossel, E. Baumann, G. W. Truong, F. Giorgetta, C. Sweeney, N. R. Newbury, K. Prasad, *et al.*, Regional trace-gas source attribution using a field-deployed dual frequency comb spectrometer, Optica **5**, 320 (2018).

[20] I. Coddington, W. C. Swann, and N. R. Newbury, Coherent Multiheterodyne Spectroscopy Using Stabilized Optical Frequency Combs, Phys. Rev. Lett. **100**, 013902 (2008).

[21] I. Coddington, W. C. Swann, and N. R. Newbury, Coherent dual-comb spectroscopy at high signal-to-noise ratio, Phys. Rev. A **82**, 043817 (2010).

[22] L. C. Andrews and R. L. Phillips, *Laser Beam Propagation Through Random Media*, 2nd ed. (SPIE, Bellingham, Washington, United States, 2005).

[23] R. L. Fante, Electromagnetic beam propagation in turbulent media, Proc. IEEE **63**, 1669 (1975).

[24] A. Ishimaru, *Wave Propagation and Scattering in Random Media* (Academic press, New York, 1978), Vol. 2.

[25] L. C. Sinclair, F. R. Giorgetta, W. C. Swann, E. Baumann, I. Coddington, and N. R. Newbury, Optical phase noise from atmospheric fluctuations and its impact on optical time-frequency transfer, Phys. Rev. A **89**, 023805 (2014).

[26] G. I. Taylor, The spectrum of turbulence, Proc. R. Soc. London, Ser. A **164**, 0476 (1938).

[27] G. Rieker, F. Giorgetta, I. Coddington, W. Swann, L. Sinclair, C. Cromer, E. Baumann, A. Zolot, and N. Newbury, in *Optical Instrumentation for Energy and Environmental Applications* (Optica Publishing Group, Tucson, Arizona, United States, 2013), pp. ET2A. 2.

[28] P. Giaccari, J. D. Deschenes, P. Saucier, J. Genest, and P. Tremblay, Active Fourier-transform spectroscopy combining the direct rf beating of two fiber-based mode-locked lasers with a novel referencing method, Opt. Express **16**, 4347 (2008).

[29] J. Roy, J. D. Deschenes, S. Potvin, and J. Genest, Continuous real-time correction and averaging for frequency comb interferometry, Opt. Express **20**, 21932 (2012).

[30] W. P. Zhang, X. Y. Chen, X. J. Wu, Y. Li, and H. Y. Wei, Adaptive cavity-enhanced dual-comb spectroscopy, Photonics Res. **7**, 883 (2019).

[31] C. D. Boone, K. A. Walker, and P. F. Bernath, Speed-dependent Voigt profile for water vapor in infrared remote sensing applications, J. Quant. Spectrosc. Radiat. Transfer **105**, 525 (2007).

[32] X. Y. Chen, W. P. Zhang, Y. J. Zhang, M. J. Lu, Y. Li, and H. Y. Wei, Segment-resolved gas concentration measurements by a time domain multiplexed dual comb method, Sensors **20**, 1566 (2020).

[33] S. D. Humphries, A. R. Nehrir, C. J. Keith, K. S. Repasky, L. M. Dobeck, J. L. Carlsten, and L. H. Spangler, Testing carbon sequestration site monitor instruments using a controlled carbon dioxide release facility, Appl. Opt. **47**, 548 (2008).

[34] F. Keilmann, C. Gohle, and R. Holzwarth, Time-domain mid-infrared frequency-comb spectrometer, Opt. Lett. **29**, 1542 (2004).

[35] A. Schliesser, N. Picque, and T. W. Hansch, Mid-infrared frequency combs, Nat. Photonics **6**, 440 (2012).

[36] G. Ycas, F. R. Giorgetta, E. Baumann, I. Coddington, D. Herman, S. A. Diddams, and N. R. Newbury, High-coherence mid-infrared dual-comb spectroscopy spanning 2.6 to 5.2 μm, Nat. Photonics **12**, 202 (2018).

[37] L. A. Sterczewski, J. Westberg, and G. Wysocki, Computational coherent averaging for free-running dual-comb spectroscopy, Opt. Express **27**, 23875 (2019).

[38] A. Weiner, *Ultrafast optics* (John Wiley & Sons, Hoboken, New Jersey, United States, 2011).